

Rational Design Heterobilayers Photocatalysts for Efficient Water Splitting Based on 2D Transition-Metal Dichalcogenide and Their Janus

Nguyen Tran Gia Bao,^{†,||} Ton Nu Quynh Trang,^{†,||} Nam Thoai,^{‡,||} Phan Bach Thang,^{¶,||} Vu Thi Hanh Thu,^{*,†,||} and Nguyen Tuan Hung^{*,§}

[†]*Faculty of Physics and Physics Engineering, University of Science, Ho Chi Minh City 700000, Viet Nam*

[‡]*Ho Chi Minh City University of Technology, Ho Chi Minh City 700000, Viet Nam*

[¶]*Center for Innovative Materials and Architectures (INOMAR), Ho Chi Minh City 700000, Viet Nam*

[§]*Frontier Research Institute for Interdisciplinary Sciences, Tohoku University, Sendai, 980-8578 Japan*

^{||}*Vietnam National University, Ho Chi Minh City 700000, Viet Nam*

E-mail: vththu@hcmus.edu.vn; nguyen.tuan.hung.e4@tohoku.ac.jp

Abstract

Direct Z-scheme heterostructures with enhanced redox potential are increasingly regarded as promising materials for solar-driven water splitting. This potential arises from the synergistic interaction between the intrinsic dipoles in Janus materials and the interfacial electric fields across the layers. In this study, we explore the photocatalytic potential of 2D two-dimensional (2D) Janus transition metal dichalcogenide (TMDC) heterobilayers for efficient water splitting. Utilizing density functional theory (DFT)

calculations, we first screen these materials based on key properties such as band gaps and the magnitude of intrinsic electric fields to identify promising candidates. We then evaluate additional critical factors, including carrier mobility and surface chemical reactions, to fully assess their performance. The intrinsic dipole moments in Janus materials generate built-in electric fields that enhance charge separation and reduce carrier recombination, thereby improving photocatalytic efficiency. Furthermore, we employ the Fröhlich interaction model to quantify the mobility contributions from the longitudinal optical phonon mode, providing detailed insights into how carrier mobility, influenced by phonon scattering, affects photocatalytic performance. Our results reveal that several Janus-TMDC heterobilayers, including WSe₂-SWSe, WSe₂-TeWSe, and WS₂-SMoSe, exhibit strong absorption in the visible spectrum and achieve solar-to-hydrogen (STH) conversion efficiencies of up to 33.24%. These findings demonstrate the potential of Janus-based Z-scheme systems to overcome existing limitations in photocatalytic water splitting by optimizing the electronic and structural properties of 2D materials. This research highlights a viable pathway for advancing clean energy generation through enhanced photocatalytic processes.

Keywords

Janus TMDC, photocatalyst, water-splitting, carrier mobility, Fröhlich interaction

1 Introduction

Due to escalating environmental pollution and energy challenges, the search for alternative energy sources has gained significant attention in the modern era. Hydrogen energy is increasingly regarded as an innovative technology for the future, providing the dual advantages of being both clean and renewable.¹⁻³ Photocatalytic water splitting has garnered significant attention in global scientific and industrial communities, which convert solar energy through the splitting process of water to H₂ energy. This utilization of solar light energy is accelerat-

ing the carbon neutralization process in the world.⁴ The photocatalytic technique is based on generating charge carriers within a photocatalyst system under suitable light irradiation. Therefore, the primary challenge is discovering a highly efficient photocatalyst that exhibits favorable photoelectronic and optical properties for STH energy conversion.^{5,6} Maximizing the efficiency of photocatalytic hydrogen generation depends on the control optimization of the critical parameters, including i) an optimal band gap and appropriately aligned conduction and valence band of the photocatalyst to effectively harvest visible light and facilitate the redox reactions required for water splitting; ii) a high surface area and well-engineered morphology, alongside a crystalline structure, enhancing light absorption and efficiently promoting charge mobility; iii) suppression of electron-hole recombination and enhanced charge carrier mobility for efficient charge transport to reactive sites; iv) reaction conditions, including pH, temperature, and the incorporation of sacrificial agents.⁵⁻⁸

Among the various photocatalysts, two-dimensional (2D) materials offer many favorable properties, such as large surface area, quantum confinement effects, strong light absorption enhanced charge separation, and structural flexibility.⁹⁻¹² One of the standout features of 2D materials is their planar structure, which offers a high density of surface atoms and ample space for integration with co-catalysts. This results in more available active sites for catalytic reactions, and the potential creates new active sites, enhancing overall catalytic efficiency.¹³ Additionally, the significantly reduced thickness of 2D materials enables charge carriers to travel shorter distances to reach the surface. This leads to decreasing electron-hole recombination and preserves more charge carriers for surface reactions. These unique characteristics make 2D materials promising candidates for improving the performance of photocatalytic systems,¹³ in which TMDC materials have been considered as the most potential applicant due to possessing efficient visible light absorption and high charge carrier mobility enhancing charge separation. The TMDCs have demonstrated good chemical stability and robust light-matter interactions, further improving their efficacy in light-driven processes. Despite these strengths, TMDCs are facing plausible limitations in photocatalytic hydrogen genera-

tion due to high exciton recombination and strong electrostatic coulomb interactions, leading to inefficient photogenerated charge carriers.^{14,15} In comparison with conventional TMDCs, Janus TMDCs include different chalcogen atoms, breaking the out-of-plane symmetry.¹⁶ Thus, the Janus TMDCs will create out-of-plane dipoles between the top and bottom layers that could generate an intrinsic electric field and enhance the photocatalytic performance in Janus-TMDCs.¹⁷⁻¹⁹

Based on the above reasons, the heterobilayers combining TMDCs and their Janus materials that have been successfully synthesized^{20,21} could benefit photocatalytic water splitting. In monolayer 2D material, both the hydrogen evolution reaction (HER) and the oxidation evolution reaction (OER) occur on the same surface of the 2D material, resulting in a higher recombination rate of photogenerated charge carriers.^{5,6} A promising solution to this problem is the van der Waals (vdW) heterobilayers of two semiconductor layers. In particular, the valence band maximum (VBM) and conduction band minimum (CBM) are integrated into both semiconductor sides, which are known as type II and Z-scheme heterostructure systems. A distinct behavior of the Z-scheme and type-II heterostructures is their unique electronic structure. Notably, the Z-scheme junction features a suitable band alignment and a wide directional built-in electric field. As a result, photogenerated charge carriers with a large redox potential are well-preserved and spatially separated within the Z-scheme heterostructures. Combining two narrow band gap semiconductors into a Z-scheme system could solve the challenge of a single platform or type-II junctions, where strong redox ability and light absorption region may not be obtained simultaneously.^{22,23} This configuration allows HER and OER activity on separate surfaces. On the other hand, the heterobilayer with the Janus structure generates an intrinsic electric field, which not only enhances the photocatalytic performance but also accelerates the reaction kinetics by forming synergistic surface properties that allow selective adsorption of water molecules on each surface.²⁴⁻²⁷ Moreover, the configuration of the heterobilayer can determine whether photogenerated carriers follow a Z-scheme or a traditional type-II pathway.²⁷ However, the diversity of possible

Janus-TMDC combinations in heterobilayers poses a significant challenge in determining the optimal configuration for photocatalytic water splitting. In this study, we provide a theoretical framework for rapidly identifying effective Janus-TMDC pairs through a top-down approach: candidates are initially filtered based on band alignment, and further refinement follows as needed. Another key challenge is the intrinsic polarization of Janus materials, which uniquely affects their electrical mobility. However, this factor is often neglected in previous Janus or TMDC studies for photocatalytic.^{1,28,29} To address this, we have adopted Fröhlich interaction model^{28,30} to account for the mobility adjustments in Janus heterostructures accurately.

In this paper, we investigate the photocatalytic properties of the 20 configurations Janus-XMY/TMDC-NZ₂ heterobilayers, where M,Z = Mo,W; and X,Y,Z are chalcogenide elements S, Se, or Te ($X \neq Y$). Using density functional theory (DFT) calculations, our study focuses on how the interfacial side of the Janus materials (i.e., S, Se, or Te atomic layers) and the different combinations with the TMDCs influence the intrinsic built-in electric field developed across them, affecting their band gap energy, CBM and VBM levels, type of configuration, and particularly the band alignment type suitable for photocatalytic water splitting reactions. Several critical properties closely associated with water-splitting performance, such as STH efficiency, exciton binding energy, charge transport, and surface chemical reactions, are thoroughly evaluated. The findings from this research can aid in selecting and designing materials for constructing efficient photocatalysts and in determining the appropriate side of Janus structures and suitable combinations of Janus and TMDC for achieving high-yield photocatalytic reactions.

2 Theoretical Approach and Computational Details

In this research, we employed DFT for calculations using the Quantum ESPRESSO package.³¹⁻³³ The generalized gradient approximation (GGA) with the Perdew-Burke-Ernzerhof

(PBE) exchange-correlation functional was utilized as implemented in the standard solid-state pseudopotentials (SSSP) library.³⁴⁻³⁶ Van der Waals interactions were incorporated using the Grimme DFT-D2 method.³⁷⁻³⁹ To address the underestimation by PBE in predicting band edge positions and band gaps, we used the Heyd-Scuseria-Ernzerhof (HSE) hybrid-functional with a mixing parameter 25%.^{40,41} The kinetic cutoff energy for wavefunctions (E_{cut}) was set to 800 eV, and the Monkhorst-Pack k-point grid was set to $12 \times 12 \times 1$ for PBE and $6 \times 6 \times 1$ for HSE based on the convergence test. All structures were fully relaxed using the BFGS scheme,⁴² with convergence criteria for force and energy differences set to 1×10^{-4} eV/Å and 1×10^{-8} eV, respectively. To prevent interlayer interactions, a relatively large vacuum layer of 30 Å was considered along the z -direction. To examine the Gibbs free energy and the mobility of the hydrogen atom, we adopted a $3 \times 3 \times 1$ supercell with 54 atoms. For the carrier mobility calculation, a rectangle $\sqrt{3} \times 1 \times 1$ supercell was used to obtain the effective mass of carriers along x - and y -directions. The Wannier90 code and the VESTA software were used for pre-processing and post-processing.^{43,44}

3 Results and Discussion

3.1 Geometric and Electronic Structures

The Janus-TMDC heterobilayers have many configurations by selecting the atoms at the interface between two layers. Replacement of these atoms results in changes in the difference in electronegativity between layers, which, in turn, modifies their optoelectrical properties and influences the photocatalytic capabilities of the material. Based on this concept, Janus MoSSe, WSSe, and their heterobilayers with TMDC, such as MoSSe-MoS₂, have already been successfully synthesized.^{20,21} Following these achievements, recent theoretical research has focused on other Janus-type materials based on molybdenum (Mo) and tungsten (W).⁴⁵⁻⁵⁰ Thus, we selected Mo and W as the metals of interest because of their promising possibilities for future synthesis and applications in water splitting. For the chalcogenides, we used

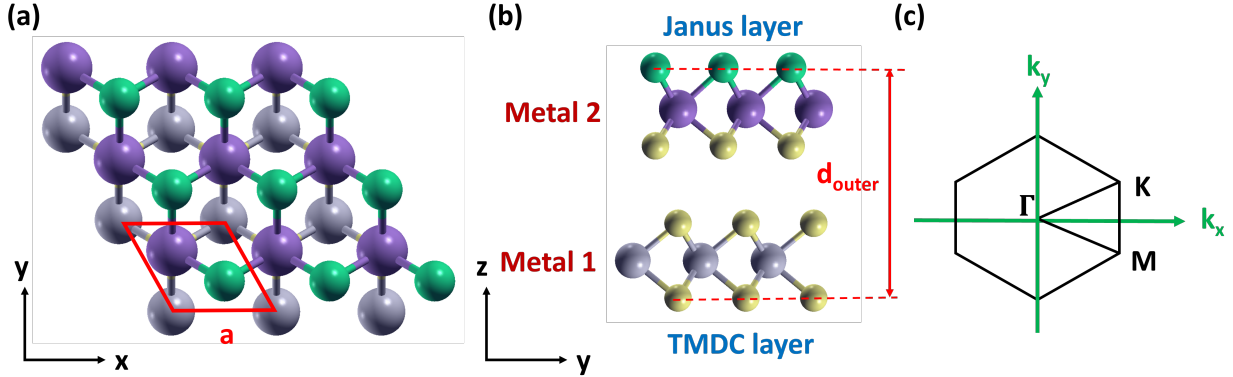


Figure 1: Visual representations of the vdW Janus-TMDC structure and its Brillouin zone: (a) top view; (b) side view; (c) Brillouin zone indicating high-symmetry points.

combinations of sulfur (S), selenium (Se), and tellurium (Te), resulting in the formation of 2D vdW structures comprising conventional TMDC and Janus materials.

The geometric structures of these 20 materials were designed based on the previously synthesized AA stacking mode of the MoSSe-MoS₂ structure, systematically replacing the metal and chalcogenide atoms, as shown in Figure 1. The optimized lattice parameters are listed in Table 1. We note that the structures of MoS₂-TeMoSe and WS₂-TeWSe did not converge during the optimization calculations, indicating that these configurations are unstable. This instability can be attributed to the significant differences in electronegativity between the S and Te atoms.

3.2 Photocatalytic characteristic

After completion of structural optimizations, we evaluated the potential of 18 materials as photocatalysts (see Table S1 in Supporting Information). To determine the electronic properties critical for photocatalytic activity, we performed partial energy band structure for 18 material combinations, in which the partial band structures show the contributions of individual layers in the heterostructures to the electronic states near the band edges (see Figure S1, Supporting Information). By projecting the electronic states onto the atomic orbitals of the Janus and TMDC layers, we identified which layers predominantly contribute

to the VBM and CBM. This approach allowed us to classify the materials into Type I band alignment, where both the VBM and CBM are contributed by the same layer, or Type II alignment and Z-scheme alignment, where they are contributed by different layers, based on the spatial localization of their VBM and CBM.

As shown in Figure S1 (Supporting Information), 11 materials exhibit a direct band gap, with both the CBM and the VBM located at the K point of the Brillouin zone. While 7 materials show the indirect band gap with the VBM is found along the K- Γ path. The calculated band gap energies for all materials are summarized in Table S1 (Supporting Information), providing a detailed comparison across the different structures. Here, we employed the HSE hybrid functional for all materials to correct the band gap values, as the commonly used generalized gradient approximation with the GGA-PBE functional tends to underestimate the energy band gap.⁴²

To be considered as a photocatalyst for water splitting, the theoretical band gap should be larger than 1.23 eV to overcome the reduction and oxidation potential of H₂O.^{1,51} However, due to the difference in electrostatic potential between the layers contributing to the VBM and CBM, even materials with smaller band gaps can act as photocatalysts. As shown in Table S1 (Supporting Information), the materials with Type I band alignment, including MoSe₂-SeMoTe, WSe₂-SeWS, and WSe₂-SeWTe, have band gaps less than 1.23 eV. Thus, they are unsuitable for water-splitting applications.

For the remaining materials, we calculated the electrostatic potential curves, as shown in Figure S2 in Supporting Information. The calculations include a dipole correction to suppress artificial dipole fields by introducing an additional ramp-shaped potential.⁴² The intrinsic electric field generated by the Janus layer in the heterostructure results in a significant potential difference between the two layers, leading to a difference in work function ($\Delta\Phi$) as calculated and presented in Table 1. Note that $\Delta\Phi$ is determined by taking the difference

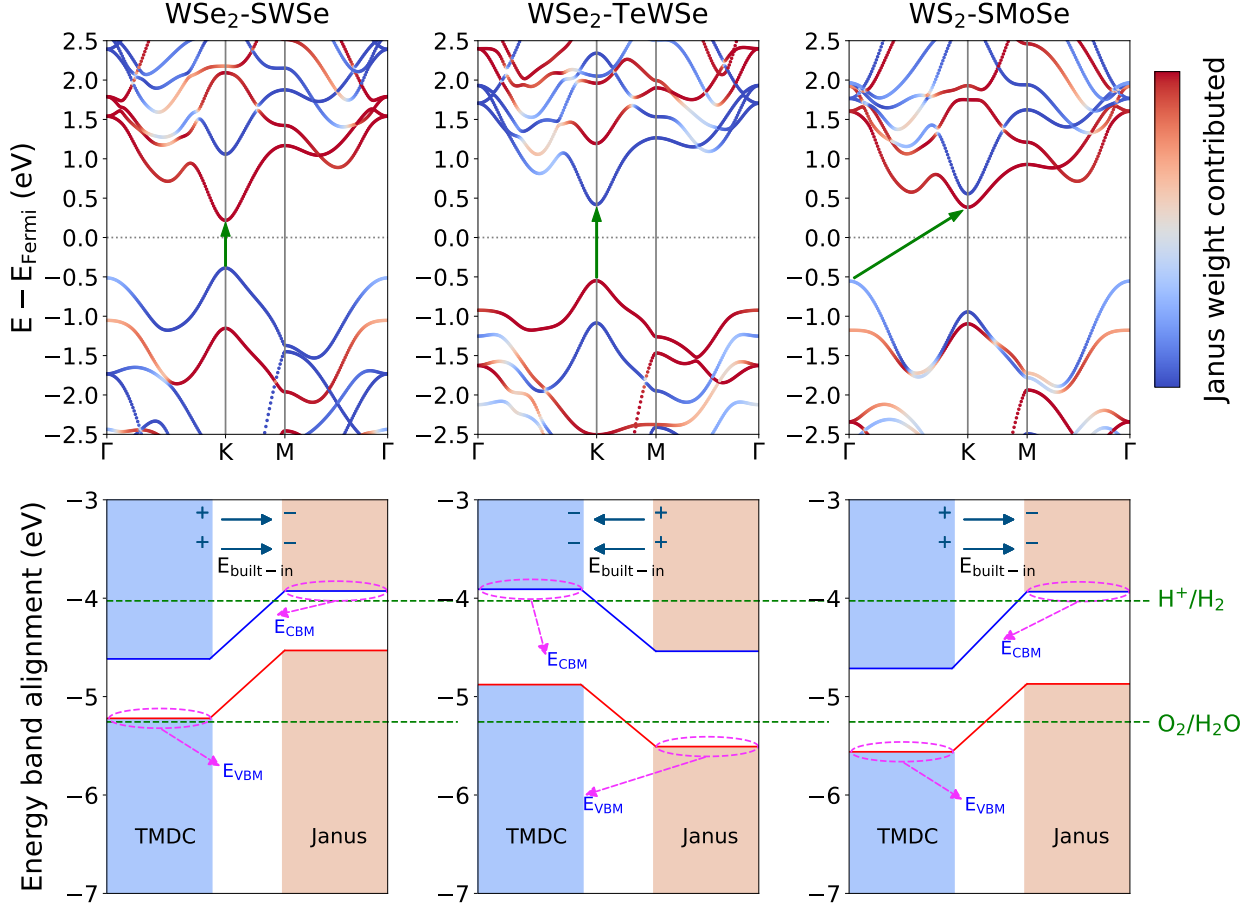


Figure 2: HSE band structure and band alignment at pH = 7 for selected Janus-TMDC heterobilayers: WSe₂-SWSe, WSe₂-TeWSe, and WS₂-SMoSe.

between the work functions of the TMDC and Janus layers, following this equation:¹⁴

$$\Delta\Phi = V_{\text{TMDC}} - V_{\text{Janus}}. \quad (1)$$

The band alignment plays a critical role in determining the photocatalytic properties of Janus-TMDC heterobilayers. When the work function difference between the layers, denoted as $\Delta\Phi$, is positive ($\Delta\Phi > 0$), this indicates that the vacuum level of the TMDC layer is higher than that of the Janus layer. In such a configuration, the TMDC layer predominantly contributes to the VBM, while the Janus layer largely influences the CBM. This arrangement leads to a Z-scheme band alignment, which effectively broadens the separation between the CBM and VBM, enhancing charge carrier separation and improving photocatalytic activity

Table 1: Calculated band gap energies, work function differences, and effective band gaps for various Janus-TMDC heterobilayers.

Sample	E_g (eV)	$\Delta\Phi$ (eV)	Alignment type	E_{eff} (eV)
MoS ₂ -SeMoTe	0.315	0.82	II	-
MoS ₂ -TeMoSe	-	-	-	-
MoSe ₂ -SeMoTe	1.044	0.84	I	1.044
MoSe ₂ -TeMoSe	0.481	-0.6	Z-scheme	1.081
MoS ₂ -SMoSe	1.313	0.82	I	1.313
MoS ₂ -SeMoS	0.68	-0.64	Z-scheme	1.32
MoSe ₂ -SMoSe	0.494	0.71	Z-scheme	1.204
MoSe ₂ -SeMoS	1.111	-0.73	I	1.111
WS ₂ -SWSe	1.437	0.79	I	1.437
WS ₂ -SeWS	0.815	-0.66	Z-scheme	1.475
WSe ₂ -SWSe	0.604	0.69	Z-scheme	1.294
WSe ₂ -SeWS	1.211	-0.7	I	1.211
WS ₂ -SeWTe	0.411	0.93	II	-
WS ₂ -TeWSe	-	-	-	-
WSe ₂ -SeWTe	1.103	0.8	I	1.103
WSe ₂ -TeWSe	0.969	-0.63	Z-scheme	1.599
MoS ₂ -SWSe	1.562	0.83	II	0.732
MoS ₂ -SeWS	0.952	-0.58	Z-scheme	1.532
WS ₂ -SMoSe	0.937	0.79	Z-scheme	1.717
WS ₂ -SeMoS	1.517	-0.71	Z-scheme	2.227

(e.g., WSe₂-SWSe and WS₂-SMoSe, as shown in Figure 2). Conversely, when $\Delta\Phi$ is negative ($\Delta\Phi < 0$), meaning the vacuum level of the Janus layer is higher than that of the TMDC layer, the Janus layer mainly contributes to the VBM, and the TMDC layer to the CBM. This configuration also results in a Z-scheme alignment (e.g., WSe₂-TeWSe, as shown in Figure 2).

In cases where $\Delta\Phi$ is negligible or does not meet the conditions above, the system exhibits a type II band alignment. The effective band gap in a Z-scheme configuration can be expressed as $E_{\text{eff}} = E_g + \Delta\Phi$, where E_g represents the intrinsic band gap, and $\Delta\Phi$ reflects the built-in potential difference at the heterostructure interface. Materials with $E_{\text{eff}} > 1.23$ eV are considered promising candidates for photocatalytic applications, and their performance is further evaluated through calculations of STH efficiency. The E_{eff} values for the materials studied are summarized in Table 1.

3.3 Solar to Hydrogen Conversion Efficiency (STH)

After screening all possible materials for their ability to initialize water splitting, we identified 9 materials (see Table 2) with an effective band gap greater than 1.23 eV, indicating that these materials can potentially straddle the whole redox potential of H₂O. The redox potential of water depends on pH and can be described as follows:

$$E_{\text{H}^+/\text{H}_2} = 0 - 0.059 \times \text{pH}, \quad (2)$$

and

$$E_{\text{O}_2/\text{H}_2\text{O}} = 1.23 - 0.059 \times \text{pH}. \quad (3)$$

Determining the appropriate pH for water splitting is crucial for optimizing the performance of photocatalysts. Therefore, we analyzed the band alignment of the selected materials for the redox potentials at pH = 0 and 7, as illustrated in Figure S3 (Supporting Information). We find that some materials require solution pH < -2, indicating highly acidic conditions, which limits their practical application.^{52,53} Therefore, these materials are excluded from the STH efficiency calculations. Only materials capable of splitting water at pH = 0 and 7 are considered for the STH efficiency evaluation, with the relevant material information provided in Table 2. It is noted that the VBM of WSe₂-SWSe is slightly higher than the OER potential. Therefore, at pH = 7, this material exhibits only the hydrogen evolution half-reaction during photocatalysis.

The STH efficiency η_{STH} of the selected materials were calculated using the following expression:¹

$$\eta_{\text{STH}} = \eta_{\text{abs}} \times \eta_{\text{cu}} \times \frac{\int_0^\infty P(h\omega)d(h\omega)}{\int_0^\infty P(h\omega)d(h\omega) + \Delta\Phi \int_{E_g}^\infty \frac{P(h\omega)}{h\omega}d(h\omega)}, \quad (4)$$

where η_{abs} is the light absorption efficiency, η_{cu} is the carrier utilization efficiency, E_g is the band gap energy, $\Delta\Phi$ is the electric potential difference, and $P(h\omega)$ represents the AM1.5G

Table 2: STH conversion efficiencies, including overpotentials (χ_{H} and χ_{O}), absorption (η_{abs}) and carrier utilization efficiencies (η_{cu}) for selected materials.

Material	χ_{H}	χ_{O}	η_{abs}	η_{cu}	η_{STH}
WSe ₂ -SWSe	0.1	0.01	96.63%	45.50%	30.71%
WSe ₂ -TeWSe	0.12	0.25	87.08%	46.45%	30.72%
WS ₂ -SMoSe	0.09	0.39	88.54%	52.77%	33.24%
WS ₂ -SeMoS	0.27	0.73	60.68%	57.62%	29.12%
MoS ₂ -SMoSe					
MoS ₂ -SeMoS					
WS ₂ -SWSe		Require low pH (pH < 0)			
WS ₂ -SeWS					
MoS ₂ -SeWS					

solar flux at photon energy $h\omega$. The light absorption efficiency (η_{abs}) is given by

$$\eta_{\text{abs}} = \frac{\int_{E_{\text{g}}}^{\infty} P(h\omega) d(h\omega)}{\int_0^{\infty} P(h\omega) d(h\omega)}, \quad (5)$$

and the carrier utilization η_{cu} is determined by

$$\eta_{\text{cu}} = \frac{\Delta E_{\text{splitting}} \int_{E_{\text{min}}}^{\infty} \frac{P(h\omega)}{h\omega} d(h\omega)}{\int_{E_{\text{g}}}^{\infty} P(h\omega) d(h\omega)} \quad (6)$$

where $\Delta E_{\text{splitting}} = 1.23$ eV for water splitting and

$$E_{\text{min}} = \begin{cases} E_{\text{g}} & \text{for } \chi(\text{H}_2) \geq 0.2, \chi(\text{O}_2) \geq 0.6 \\ E_{\text{g}} + 0.2 - \chi(\text{H}_2) & \text{for } \chi(\text{H}_2) < 0.2, \chi(\text{O}_2) \geq 0.6 \\ E_{\text{g}} + 0.6 - \chi(\text{O}_2) & \text{for } \chi(\text{H}_2) \geq 0.2, \chi(\text{O}_2) < 0.6 \\ E_{\text{g}} + 0.8 - \chi(\text{H}_2) - \chi(\text{O}_2) & \text{for } \chi(\text{H}_2) < 0.2, \chi(\text{O}_2) < 0.6 \end{cases}, \quad (7)$$

where $\chi(\text{H}_2)$ and $\chi(\text{O}_2)$ are the overpotentials for the hydrogen and oxygen evolution reactions, respectively. It is noted that $\chi(\text{H}_2)$ is the potential difference between the CBM and the redox potential of H^+/H_2 , while $\chi(\text{O}_2)$ is the potential difference between the VBM and the redox potential of $\text{O}_2/\text{H}_2\text{O}$, as shown in Figure 2. Our calculated results, presented in Table 2, show that the selected materials exhibit remarkable photocatalytic efficiencies

and exceed the conventional theoretical limit of 18%.⁵⁴ In particular, WS₂-SMoSe achieves an η_{STH} of 33.24%. In comparison, materials reported in previous studies, such as Penta-PdSeTe (29.71%),⁵⁵ Janus γ -GeSSe (28.78%),¹ and SPtGeAs₂ (30.74%),⁵⁶ show competitive but lower efficiencies.

The exceptional performance of WS₂-SMoSe and other materials in Table 2 can be attributed to its optimal electronic structure and favorable band alignment, which facilitate efficient light absorption and charge carrier utilization. The light absorption efficiency η_{abs} is particularly high for materials with smaller band gaps, as shown in Equation 5. WSe₂-SWSe with a band gap of 0.604 eV exhibits an outstanding η_{abs} of 96.63%, which allows it to absorb a broader spectrum of solar radiation compared to traditional photocatalysts with a standard band gap of 1.23 eV. It is important to note that Equation 5 assumes the absorbance as a step function zero for photon energies below the band gap and unity for energies above it. This simplification may lead to underestimating η_{abs} , particularly at lower photon energies. Therefore, while the calculated η_{abs} provides valuable insights, it may be more accurate for materials with high photon energy absorption.

3.4 Carrier mobility

The relationship between carrier mobility and photocatalytic efficiency is essential in determining the performance of photocatalysts. After the electron-hole pairs are separated, the free photoexcited carriers need to migrate to the chemical active sites for water splitting. Higher mobility enables these charge carriers to travel faster and further, reducing the probability of recombination before they can reach the reactive surface sites.⁵⁷⁻⁶⁰ Mobility is primarily limited by phonon scattering, which impedes the movement of charge carriers. Traditional approaches to calculating mobility, such as deformation potential theory (DPT), focus on the scattering caused by longitudinal acoustic (LA) phonons.^{14,56,60} However, recent studies, such as Cheng and Liu have demonstrated that this method often underestimates the influence of longitudinal optical (LO) phonon scattering, particularly in Janus materials

with strong polar effects.

The carrier mobility μ_{LA} due to the LA phonon scattering within the DPT theory is given as follows:^{1,59}

$$\mu_{\text{LA}} = \frac{e\hbar^3 C_{2\text{D}}}{k_{\text{B}} T m_{x(y)}^* m_{\text{d}} E_{\text{d}}^2}, \quad (8)$$

where the effective masses along the zigzag (x) and armchair (y) directions are represented by m_x^* and m_y^* , respectively, and the average effective mass given by $m_{\text{d}} = \sqrt{m_x^* m_y^*}$. A $\sqrt{3} \times 1$ supercell (see Figure S4 in Supporting Information) is used to compute m_x^* and m_y^* . The in-plane Young's modulus, $C_{2\text{D}}$, is defined as:^{1,59}

$$C_{2\text{D}} = \frac{\partial^2 E_{\text{total}}}{\partial \varepsilon^2} / S_0, \quad (9)$$

where E_{total} is the total energy after applying a uniaxial strain (with strain $\varepsilon = \Delta l/l_0$), and S_0 is the equilibrium area of the system (see Figure S5, Supporting Information). The deformation potential constant, E_{d} , is given by

$$E_{\text{d}} = \frac{\Delta E}{\varepsilon}, \quad (10)$$

where ΔE is the shift in the energy level of either the CBM or the VBM relative to the vacuum level (see Figure S6 in Supporting Information). The calculated parameters at room temperature ($T = 300$ K) are presented in Table 3.

It is important to note that many 2D TMDCs exhibit mobility limited by not only LA but also LO phonon scattering.²⁸ The LO phonon scattering is closely linked to the Born effective charge, which reflects the degree of electric polarization change due to atomic vibrations. Thus, a large Born effective charge correlates with stronger carrier scattering, leading to reduced mobility. This critical insight highlights the need to go beyond DPT to accurately assess the intrinsic mobility of Janus-TMDC heterostructures when LO phonon scattering could play a substantial role. In the present study, the Fröhlich interaction model^{28,30} is

Table 3: Material properties of selected Janus-TMDC heterobilayers, including effective masses (m^*), deformation potentials (E_d), and calculated carrier mobilities (μ_{LA}).

Sample	Direction	Carrier	m^*/m_0	E_d (eV)	C_{2D} (N/m)	μ_{LA} (cm ² /V·s)
WSe ₂ -S ₂ WSe	zigzag	h	0.401	2.26	218.7755	5085.70
		e	0.225	2.70		11120.74
	armchair	h	0.499	2.18	201.1680	4038.86
		e	0.290	2.64		8298.47
WSe ₂ -TeWSe	zigzag	h	0.611	2.52	212.9836	1735.10
		e	0.257	2.16		13274.89
	armchair	h	0.743	2.46	199.0206	1399.13
		e	0.316	2.26		9215.51
WS ₂ -SMoSe	zigzag	h	0.252	4.70	245.0984	3499.11
		e	0.343	4.70		1697.92
	armchair	h	0.285	4.78	229.1263	2796.32
		e	0.480	4.34		1330.22

employed to quantify the mobility contributions from the LO phonon mode. The total scattering rate near the band edges can be written as

$$\frac{1}{\tau_{\text{LO}}} = \frac{e^2 n_{h\omega}}{M_M M_{X_1} M_{X_2} S_0 d_{eff}^2 (\varepsilon \varepsilon_0)^2 (\hbar \omega)^2} \times \left[|Z_{MB}| \sqrt{M_{X_1} M_{X_2}} + |Z_{X_1}| \sqrt{M_M M_{X_2}} + |Z_{X_2}| \sqrt{M_M M_{X_1}} \right]^2, \quad (11)$$

where e is the elementary charge, $n_{h\omega}$ is the Bose-Einstein distribution at the phonon frequency at the gamma point, A is the equilibrium area, d_{eff} is the effective thickness, ε is the in-plane optical dielectric constant, and ε_0 is the dielectric constant. Additionally, M_M , M_{X_1} , and M_{X_2} are the atomic masses of the metal and the two chalcogens in the structure, while Z_{MB} , Z_{X_1} , and Z_{X_2} are the Born effective charges of the metal and the two chalcogen atoms (see Table S2 in Supporting Information for reference). Thus, the mobility contributed by the LO phonon mode is given by

$$\mu_{\text{LO}} = |e| \tau_{\text{LO}} / m^*. \quad (12)$$

In Janus-TMDC heterobilayers, two distinct LO phonon modes, LO1 and LO2, corre-

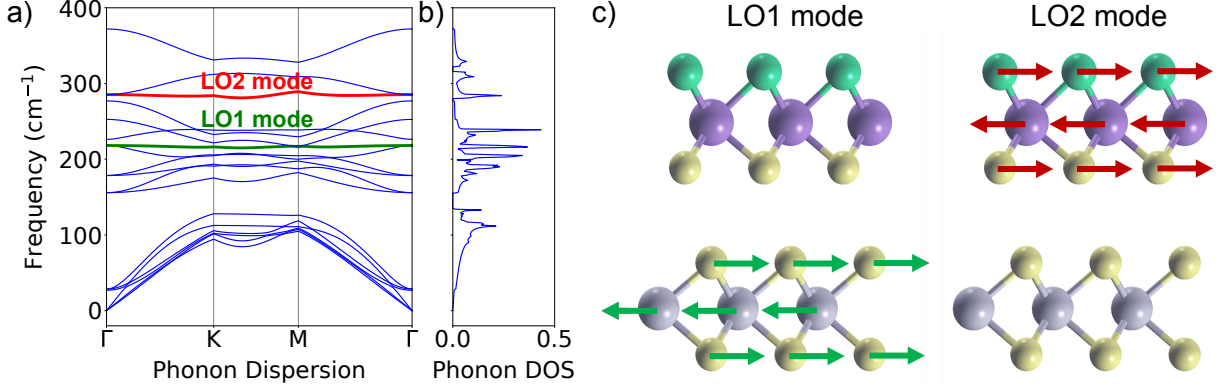


Figure 3: Phonon properties of WSe₂-SWSe (a) Phonon dispersion, (b) Phonon density of state (DOS), and (c) the vibrations of the LO1 and LO2 phonon modes at Γ point.

spond to the vibrations of the TMDC and Janus layers, respectively, as shown in Figure 3. The calculated mobilities for μ_{LO1} and μ_{LO2} are provided in Table 4. Then the total mobility μ_{total} is then determined using Matthiessen's rule as follows:²⁸

$$\frac{1}{\mu_{\text{total}}} = \frac{1}{\mu_{\text{LO1}}} + \frac{1}{\mu_{\text{LO2}}} + \frac{1}{\mu_{\text{LA}}}. \quad (13)$$

The calculated μ_{LO1} , μ_{LO2} , and μ_{total} are listed in Table 4. Our results reveal that LO phonon scattering significantly limits mobility in Janus-TMDC heterobilayers, which leads to lower carrier mobility compared to those predicted by DPT alone (see Table 3).

3.5 Optical properties

The optical property is another factor in determining the effectiveness of semiconductor materials as optoelectronic devices. Additionally, photocatalysts with strong light absorption capabilities will perform more efficiently.

The optical properties of WSe₂-SWSe, WSe₂-TeWSe, and WS₂-SMoSe are calculated by using the independent particle approximation. The absorption coefficient $\alpha(\omega)$ is obtained

Table 4: Calculated mobilities contributed by LO1 and LO2 modes (μ_{LO1} and μ_{LO2}) and combined LA and LO modes (μ_{total}).

Sample	Direction	Carrier	μ_{LO1} ($\text{cm}^2/\text{V}\cdot\text{s}$)	μ_{LO2} ($\text{cm}^2/\text{V}\cdot\text{s}$)	μ_{total} ($\text{cm}^2/\text{V}\cdot\text{s}$)
WSe ₂ -SWSe	zigzag	h	980.78	5669.29	718.07
		e	1719.25	9937.93	1295.01
	armchair	h	980.78	5669.29	692.72
		e	1719.25	9937.93	1245.67
WSe ₂ -TeWSe	zigzag	h	946.32	246.97	175.99
		e	2237.96	584.06	447.56
	armchair	h	946.32	246.97	171.81
		e	2237.96	584.06	441.01
WS ₂ -SMoSe	zigzag	h	109174.17	2137.68	1311.06
		e	72065.71	1411.08	762.48
	armchair	h	109174.17	2137.68	1198.22
		e	72065.71	1411.08	678.28

from the calculated real ε_1 and imaginary ε_2 parts of the dielectric function as follows:⁴²

$$\alpha(\omega) = \frac{\sqrt{2}\omega}{c} \left\{ \sqrt{\varepsilon_1^2(\omega) + \varepsilon_2^2(\omega)} - \varepsilon_1(\omega) \right\}^{1/2}. \quad (14)$$

Here, the values of ε_1 and ε_2 are scaled by the factor h/d_0 where h represents the unit cell thickness and d_0 denotes the effective material thickness.¹⁴ The effective thickness, d_0 , is calculated using the formula: $d_0 = d_{\text{outer}} + r_{\text{atom1}} + r_{\text{atom2}}$, where d_{outer} is the distance between the two outermost atoms of the heterostructure, as illustrated in 1. The terms r_{atom1} and r_{atom2} correspond to the vdW radii of the two outermost atoms.⁶¹

The absorption spectra exhibit strong anisotropic behavior, with $\alpha(\omega)$ along the in-plane (E_{\parallel}) reaching up to $0.84 \times 10^6 \text{ cm}^{-1}$ in the visible light region for WS₂-SMoSe and WSe₂-TeWSe, and $0.77 \times 10^6 \text{ cm}^{-1}$ for WSe₂-SWSe. These values surpass those of monolayer γ -GeSSe ($0.44 \times 10^6 \text{ cm}^{-1}$)¹ and PdSSe ($0.24 \times 10^6 \text{ cm}^{-1}$).⁶² Notably, the E_{\parallel} optical absorption differs considerably from the out-of-plane (E_{\perp}) absorption, especially within the visible spectrum. The combination of superior STH efficiency and strong light absorption across all materials highlights their potential for optoelectronic and water-splitting applications.

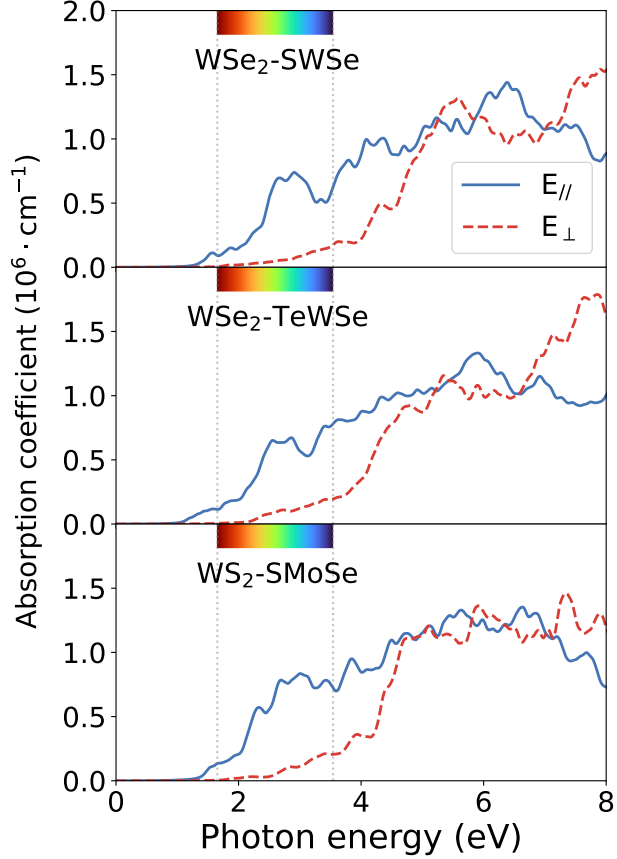


Figure 4: Optical absorption spectra along in-plane (E_{\parallel}) and out-of-plane (E_{\perp}) of WSe_2 - SWSe , WSe_2 - TeWSe , and WS_2 - SMoSe . The dashed line denotes the range of the visible light.

3.6 Hydrogen Evolution Reaction

3.6.1 Gibbs free energy steps for HER

The research indicates that the selected photocatalysts exhibit characteristics of direct Z-scheme systems, featuring appropriate band edge potentials and high efficiency. However, these properties alone do not ensure the spontaneous occurrence of the water-splitting reaction under light irradiation. To further evaluate the hydrogen evolution reaction (HER) capabilities, the Gibbs free energy change (ΔG_{H}) for hydrogen adsorption is considered a crucial factor in assessing the HER capabilities of photocatalysts. To accurately calculate the adsorption energy and minimize interactions between adjacent atoms, a $3 \times 3 \times 1$ supercell was constructed for each material, ensuring that the results reflect the behavior of isolated

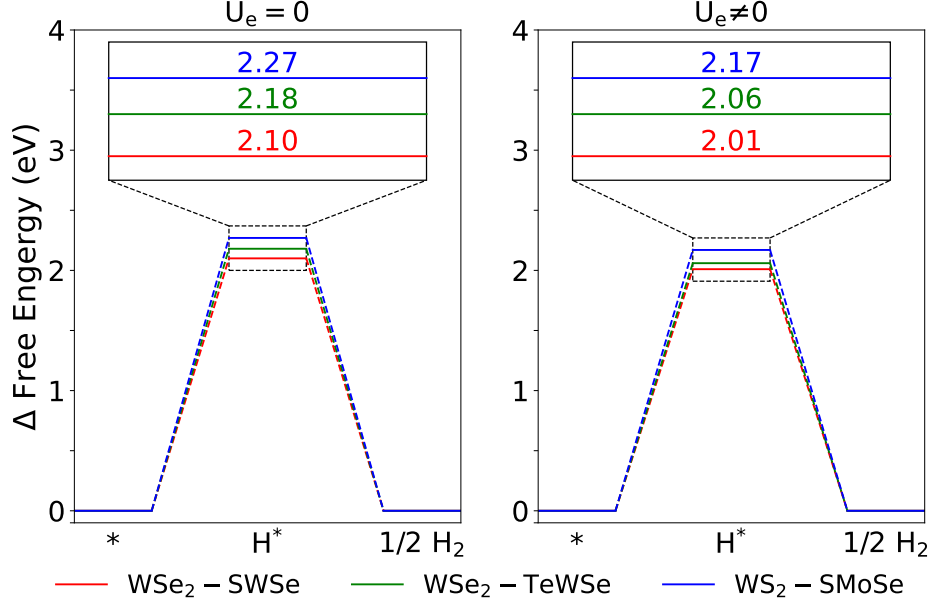


Figure 5: Calculated Gibbs free energy steps for HER under various illumination conditions.

hydrogen atoms. The Gibbs free energy change was determined using the equations:

$$\Delta G_{\text{H}} = \Delta E_{\text{H}} + 0.24 \text{ eV}, \quad (15)$$

and

$$\Delta E_{\text{H}} = E_{\text{Janus-TMDC} + \text{H}} - E_{\text{Janus-TMDC}} - \frac{1}{2}E_{\text{H}}, \quad (16)$$

where $E_{\text{Janus-TMDC} + \text{H}}$ is the total energy of the heterostructure of Janus monolayer and TMDC material with an adsorbed hydrogen atom, $E_{\text{Janus-TMDC}}$ is the energy of the bare vdW layers, and $\frac{1}{2}E_{\text{H}}$ represents the energy of a hydrogen molecule in its standard state. Building upon this, the potential provided by photogenerated electrons for HER (U_e) can be calculated using the equation $U_e = V_{\text{CB}} - 4.027$ for $\text{pH} = 7$,^{14,63} where U_e corresponds to the electron potential associated with the CBM, potentially matching the electron affinity $\chi(\text{H}_2)$ under illuminated conditions. In a dark environment, where no photogenerated electrons are available, U_e becomes zero, indicating the absence of a driving force for HER. Based on the calculations in the previous section, the U_e values for $\text{WS}_2\text{-SMoSe}$, $\text{WSe}_2\text{-TeWSe}$, and

WS₂-SMoSe under the illumination were found to be 0.10, 0.12, and 0.09 eV, respectively.

We further evaluated the HER activity at the reduction sites of WSe₂-SWSe, WSe₂-TeWSe, and again WS₂-SMoSe, with the corresponding ΔG_H values presented in Figure 5. The calculated free energy changes without an external potential are 2.10, 2.18, and 2.27 eV for these materials, respectively. These high positive values of ΔG_H indicate that spontaneous hydrogen adsorption does not occur easily, implying limited catalytic efficiency under standard conditions. Nevertheless, this behavior is similar to other well-known materials such as MoS₂, MoSe₂, WSe₂, and the Janus MoSSe materials.⁶⁴⁻⁶⁶ On the other hand, calculated free energy changes with an external potential are the ΔG_H values to 2.01, 2.06, and 2.17 eV for WSe₂-SWSe, WSe₂-TeWSe, and WS₂-SMoSe, respectively. These reduction values suggest that suitable irradiation can enhance the HER performance by decreasing the energy barrier for hydrogen adsorption. Although the ΔG_H values remain positive, indicating that the hydrogen evolution reaction is still non-spontaneous, the decreased values under light exposure or applied potential could potentially improve the catalytic performance by making hydrogen releasing more favorable.

3.6.2 Diffusion of H atom on the HER sites

To investigate H atom diffusion on the HER-active surfaces, we calculate the optimized migration pathways using a minimal energy approach.⁴⁵ The pathways and the corresponding energy profiles are shown in Figure 6, where S1 \rightarrow S2 represents H atom migration between adjacent hex-atomic-rings, and S2 \rightarrow S3 denotes migration within a single hex-atomic-ring. The migration pathways are optimized by the nudged elastic band (NEB) method⁴⁵ with a convergence criterion of 0.05 eV/Å for NEB calculations with 13 intermediate images. For WS₂-SMoSe, H migration on the SMoSe surface showed a lower energy barrier for inter-ring migration (0.199 eV) than intra-ring migration (0.216 eV). In the case of WSe₂-TeWSe, the WSe₂ surface exhibited easier migration between hex-atomic-rings (0.149 eV) than within a ring (0.286 eV). For WS₂-SMoSe, the SMoSe surface favored intra-ring migration (0.200 eV)

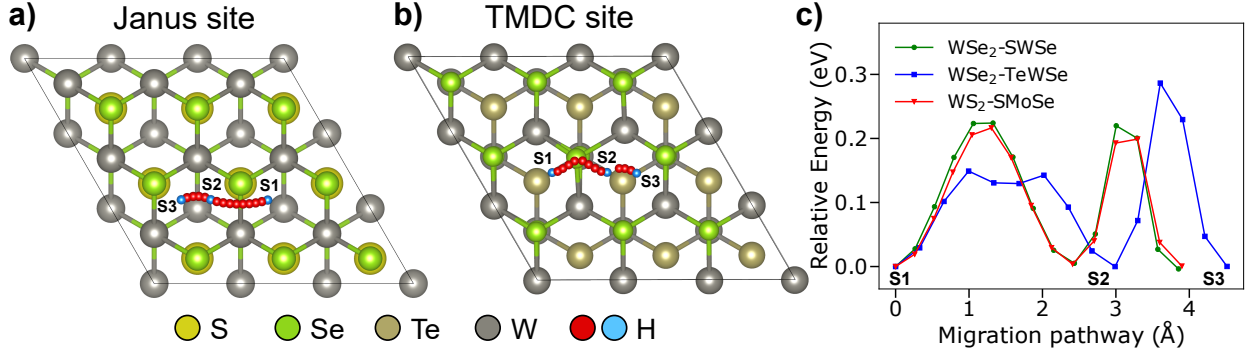


Figure 6: Migration pathways and energy profiles of a Hydrogen atom on the reduction site: (a) Janus site ($\text{WSe}_2\text{-SWSe}$ and $\text{WS}_2\text{-SMoSe}$) and (b) TMDC site ($\text{WSe}_2\text{-TeWSe}$). $\text{S1} \rightarrow \text{S2}$ indicates migration between neighboring hex-atomic-rings, while $\text{S2} \rightarrow \text{S3}$ represents migration within a hex-atomic-ring.

over inter-ring movement (0.224 eV), with this structure exhibiting a lower energy barrier compared to the other two. Compared to previously reported values,⁴⁵ the migration energy barriers of these structures are lower than those of monolayer MoSSe, which were observed at 0.32 eV for inter-ring and 0.08 eV for intra-ring migration on Se-site. This reduction suggests that these $\text{WS}_2\text{-SMoSe}$, $\text{WSe}_2\text{-TeWSe}$, and $\text{WS}_2\text{-SMoSe}$ surfaces provide more favorable diffusion pathways, which could enhance HER activity on these materials.

4 Conclusions

The findings in this study underscore the potential of Janus-TMDC heterobilayers as highly efficient photocatalysts for STH conversion. By leveraging intrinsic electric fields generated through Janus asymmetry, we achieve enhanced charge separation and minimized electron-hole recombination in Z-scheme configurations such as $\text{WSe}_2\text{-SWSe}$, $\text{WSe}_2\text{-TeWSe}$, and $\text{WS}_2\text{-SMoSe}$. These Z-scheme structures not only enable spatially separated sites for HER and OER but also provide favorable band alignment for water splitting, with $\text{WS}_2\text{-SMoSe}$ achieving the highest STH efficiency of 33.24%. In exploring the relationship between carrier mobility and photocatalytic capabilities, we use the Fröhlich interaction model to account for LO phonon scattering, revealing that mobility in Janus-TMDC heterobilayers is significantly

affected by their intrinsic polarization. Additionally, HER analysis shows that external potential effectively lowers reaction barriers, enhancing HER efficiency under illumination. Hydrogen diffusion also indicates relatively low energy barriers for H atom migration on HER-active surfaces, suggesting efficient diffusion on the WSe₂-SWSe, WSe₂-TeWSe, and WS₂-SMoSe surfaces. Overall, this work provides a comprehensive framework for selecting and designing the optimized Janus-TMDC heterobilayers for clean energy applications, presenting a promising pathway toward advancing efficient photocatalytic systems.

Acknowledgement

This work was financially supported by Vietnam National University Ho Chi Minh City (NCM2024-50-01).

Supporting Information Available

Supporting Information: Table of structural parameters and band Gap; table of Born charges, Phonon frequency, and dielectric properties; figure of HSE06-calculated band structure; figure of electrostatic potential along vacuum axis (z); figure of band alignments for water splitting at pH 0, 2, and 7; figure of PBE band structure for the effective mass calculation; figure of total energy-strain relationship in zigzag and armchair directions; figure of CBM and VBM energies under uniaxial strain; figure of Phonon dispersion and DOS.

References

- (1) Thanh, V. V.; Truong, D. V.; Tuan Hung, N. Janus γ -GeSSe monolayer as a high-performance material for photocatalysis and thermoelectricity. *ACS Appl. Energy Mater.* **2023**, *6*, 910–919.

- (2) Trang, T. N. Q.; Bao, N. T. G.; Thang, P. B.; Thu, V. T. H. Manipulating the Morphology and Charge Accumulation driven-Schottky Functionalized type II-scheme Heterojunction for Photocatalytic Hydrogen Evolution and SERS detection. *Mater. Chem. Phys.* **2024**, 129568.
- (3) Trang, T. N. Q.; Bao, N. T. G.; Doanh, T. T.; Thu, V. T. H. Multifunctional engineering on the ultrasensitive driven-dual plasmonic heterogenous dimer system of 1D semiconductor for accurate SERS sensitivity and quantitation. *J. Sci. Adv. Mater. Devices* **2024**, *9*, 100670.
- (4) Liao, G.; Li, C.; Li, X.; Fang, B. Emerging polymeric carbon nitride Z-scheme systems for photocatalysis. *Cell Rep. Phys. Sci.* **2021**, *2*, 100355.
- (5) Liu, X.; Cheng, P.; Li, S.; Liu, W. Designing a dipole-scheme heterostructure based on Janus TMDCs for highly efficient photocatalytic overall water splitting. *Adv. Mater. Interfaces* **2023**, *10*, 2300170.
- (6) Qian, G. L.; Xie, Q.; Liang, Q.; Luo, X. Y.; Wang, Y. X. Electronic properties and photocatalytic water splitting with high solar-to-hydrogen efficiency in a hBNC/Janus WSSe heterojunction: First-principles calculations. *Phys. Rev. B* **2023**, *107*, 155306.
- (7) Rahimi, K.; Moshfegh, A. Z. Interfacial Control at Janus WSSe/Triazine g-C₃N₄ Heterostructures in Developing Type-II and Z-Scheme Photocatalysts. *J. Phys. Chem. C* **2023**, *127*, 16792–16801.
- (8) Wang, Q.; Domen, K. Particulate photocatalysts for light-driven water splitting: mechanisms, challenges, and design strategies. *Chem. Rev.* **2019**, *120*, 919–985.
- (9) Wang, W.; Cheng, B.; Luo, G.; Yu, J.; Cao, S. S-scheme heterojunction photocatalysts based on 2D materials.

- (10) Ma, L.-N.; Guo, J.; Xu, W.; Yao, Y.; Cao, J.; Wei, X.-L. Two-Dimensional van der Waals β -AsP/InS Heterostructure for Photocatalysts. *128*, 18247–18254.
- (11) Wu, X.; Ling Tan, H.; Zhang, C.; Teng, Z.; Liu, Z.; Hau Ng, Y.; Zhang, Q.; Su, C. Recent advances in two-dimensional ultrathin Bi-based photocatalysts. *133*, 101047.
- (12) Tan, C.; Cao, X.; Wu, X.-J.; He, Q.; Yang, J.; Zhang, X.; Chen, J.; Zhao, W.; Han, S.; Nam, G.-H., et al. Recent advances in ultrathin two-dimensional nanomaterials. *Chem. Rev.* **2017**, *117*, 6225–6331.
- (13) Li, Y.; Gao, C.; Long, R.; Xiong, Y. Photocatalyst design based on two-dimensional materials. *Mater. Today Chem.* **2019**, *11*, 197–216.
- (14) Yuan, G.; Ma, X.; Liao, J.; Xie, T.; Xie, Q.; Yuan, Z. First-principles calculations of 2D Janus WSSiN₂ monolayer for photocatalytic water splitting. *ACS Appl. Nano Mater.* **2023**, *6*, 1956–1964.
- (15) Liu, F.; He, Y.; Liu, X.; Wang, Z.; Liu, H.-L.; Zhu, X.; Hou, C.-C.; Weng, Y.; Zhang, Q.; Chen, Y. Regulating excitonic effects in covalent organic frameworks to promote free charge carrier generation. *ACS Catal.* **2022**, *12*, 9494–9502.
- (16) Hung, N. T.; Nguyen, T.; Van Thanh, V.; Wang, S.; Saito, R.; Li, M. Symmetry breaking in 2D materials for optimizing second-harmonic generation. *J. Phys. D: Appl. Phys.* **2024**, *57*, 333002.
- (17) Yuan, H.; Su, J.; Zhang, P.; Lin, Z.; Zhang, J.; Zhang, J.; Chang, J.; Hao, Y. Tuning the intrinsic electric field of Janus-TMDs to realize high-performance β -Ga₂O₃ device based on β -Ga₂O₃/Janus-TMD heterostructures. *21*, 100549.
- (18) Albert L. Sino, P.; Lin, T.-C.; Wani, S.; Lee, L.; Chen, C.-T.; Liu, M.-J.; Kuo, Y.-Z.; Rehman, B.; Tuyen Le, K.; Wu, J.-M.; Chuang, F.-C.; Chueh, Y.-L. Controllable

- structure-engineered janus and alloy polymorphic monolayer transition metal dichalcogenides by plasma-assisted selenization process toward high-yield and wafer-scale production. *69*, 97–106.
- (19) Van Thanh, V.; Van, N. D.; Saito, R.; Hung, N. T., et al. First-principles study of mechanical, electronic and optical properties of Janus structure in transition metal dichalcogenides. *Appl. Surf. Sci.* **2020**, *526*, 146730.
- (20) Hung, N. T.; Zhang, K.; Van Thanh, V.; Guo, Y.; Puretzky, A. A.; Geohegan, D. B.; Kong, J.; Huang, S.; Saito, R. Nonlinear optical responses of Janus MoSSe/MoS₂ heterobilayers optimized by stacking order and strain. *ACS Nano* **2023**, *17*, 19877–19886.
- (21) Zhang, K.; Guo, Y.; Larson, D. T.; Zhu, Z.; Fang, S.; Kaxiras, E.; Kong, J.; Huang, S. Spectroscopic signatures of interlayer coupling in Janus MoSSe/MoS₂ heterostructures. *ACS Nano* **2021**, *15*, 14394–14403.
- (22) Liu, X.; Zhao, Y.-M.; Zhang, X.; Wang, L.; Shen, J.; Zhou, M.; Shen, L. Data-driven discovery of transition metal dichalcogenide-based *Z*-scheme photocatalytic heterostructures. *13*, 9936–9945.
- (23) Gao, X.; Shen, Y.; Liu, J.; Lv, L.; Zhou, M.; Zhou, Z.; Ping Feng, Y.; Shen, L. Developing Dipole-scheme heterojunction photocatalysts. *599*, 153942.
- (24) Cavalcante, L.; Gjerding, M.; Chaves, A.; Thygesen, K. Enhancing and controlling plasmons in Janus MoSSe–graphene based van der Waals heterostructures. *J. Phys. Chem. C* **2019**, *123*, 16373–16379.
- (25) Pang, R.; Wang, S. Dipole moment and pressure dependent interlayer excitons in MoSSe/WSSe heterostructures. *Nanoscale* **2022**, *14*, 3416–3424.
- (26) Peng, J.; Li, C.; Dong, H.; Wu, F. Intrinsic type-II van der Waals heterostructures

- based on graphdiyne and XSSe (X= Mo, W): a first-principles study. *Phys. Chem. Chem. Phys.* **2022**, *24*, 21331–21336.
- (27) Xu, X.; Jiang, X.; Gao, Q.; Yang, L.; Sun, X.; Wang, Z.; Li, D.; Cui, B.; Liu, D. Enhanced photoelectric performance of MoSSe/MoS₂ van der Waals heterostructures with tunable multiple band alignment. *Phys. Chem. Chem. Phys.* **2022**, *24*, 29882–29890.
- (28) Cheng, L.; Liu, Y. What limits the intrinsic mobility of electrons and holes in two dimensional metal dichalcogenides? *JACS* **2018**, *140*, 17895–17900.
- (29) Ju, L.; Bie, M.; Tang, X.; Shang, J.; Kou, L. Janus WSSe monolayer: an excellent photocatalyst for overall water splitting. *ACS Appl. Mater. Interfaces.* **2020**, *12*, 29335–29343.
- (30) Sohler, T.; Calandra, M.; Mauri, F. Two-dimensional Fröhlich interaction in transition-metal dichalcogenide monolayers: Theoretical modeling and first-principles calculations. *Phys. Rev. B* **2016**, *94*, 085415.
- (31) Giannozzi, P. et al. Advanced capabilities for materials modelling with QUANTUM ESPRESSO. *J. Phys. Condens. Matter* **2017**, *29*, 465901.
- (32) Giannozzi, P. et al. QUANTUM ESPRESSO: a modular and open-source software project for quantum simulations of materials. *J. Phys. Condens. Matter* **2009**, *21*, 395502 (19pp).
- (33) Giannozzi, P.; Baseggio, O.; Bonfà, P.; Brunato, D.; Car, R.; Carnimeo, I.; Cavazzoni, C.; De Gironcoli, S.; Delugas, P.; Ferrari Ruffino, F., et al. Quantum ESPRESSO toward the exascale. *J. Chem. Phys.* **2020**, *152*.
- (34) Blöchl, P. E. Projector augmented-wave method. *Phys. Rev. B* **1994**, *50*, 17953.

- (35) Prandini, G.; Marrazzo, A.; Castelli, I. E.; Mounet, N.; Marzari, N. Precision and efficiency in solid-state pseudopotential calculations. *npj Comput. Mater.* **2018**, *4*, 72.
- (36) Lejaeghere, K.; Bihlmayer, G.; Björkman, T.; Blaha, P.; Blügel, S.; Blum, V.; Caliste, D.; Castelli, I. E.; Clark, S. J.; Dal Corso, A., et al. Reproducibility in density functional theory calculations of solids. *Science* **2016**, *351*, aad3000.
- (37) Thonhauser, T.; Cooper, V. R.; Li, S.; Puzder, A.; Hyldgaard, P.; Langreth, D. C. Van der Waals density functional: Self-consistent potential and the nature of the van der Waals bond. *Phys. Rev. B* **2007**, *76*, 125112.
- (38) Thonhauser, T.; Zuluaga, S.; Arter, C.; Berland, K.; Schröder, E.; Hyldgaard, P. Spin signature of nonlocal correlation binding in metal-organic frameworks. *Phys. Rev. Lett* **2015**, *115*, 136402.
- (39) Berland, K.; Cooper, V. R.; Lee, K.; Schröder, E.; Thonhauser, T.; Hyldgaard, P.; Lundqvist, B. I. van der Waals forces in density functional theory: a review of the vdW-DF method. *Rep. Prog. Phys.* **2015**, *78*, 066501.
- (40) Heyd, J.; Scuseria, G. E.; Ernzerhof, M. Hybrid functionals based on a screened Coulomb potential. *J. Chem. Phys.* **2003**, *118*, 8207–8215.
- (41) Mostofi, A. A.; Yates, J. R.; Lee, Y.-S.; Souza, I.; Vanderbilt, D.; Marzari, N. wannier90: A tool for obtaining maximally-localised Wannier functions. *Comput. Phys. Commun.* **2008**, *178*, 685–699.
- (42) Hung, N. T.; Nugraha, A. R.; Saito, R. *Quantum ESPRESSO course for solid-state physics*; Jenny Stanford Publishing, New York, 2022.
- (43) Pizzi, G.; Vitale, V.; Arita, R.; Blügel, S.; Freimuth, F.; Géranton, G.; Gibertini, M.; Gresch, D.; Johnson, C.; Koretsune, T., et al. Wannier90 as a community code: new features and applications. *J. Phys. Condens. Matter* **2020**, *32*, 165902.

- (44) Momma, K.; Izumi, F. VESTA 3 for three-dimensional visualization of crystal, volumetric and morphology data. *J. Appl. Crystallogr.* **2011**, *44*, 1272–1276.
- (45) Lei, X.; Ouyang, C.; Huang, K. A first-principles investigation of Janus MoSSe as a catalyst for photocatalytic water-splitting. *Appl. Surf. Sci.* **2021**, *537*, 147919.
- (46) Cai, B.; Tan, J.; Zhang, L.; Xu, D.; Dong, J.; Ouyang, G. Ultrafast interfacial charge transfer and superior photoelectric conversion properties in one-dimensional Janus-MoSSe/WSe₂ van der Waals heterostructures. *Phys. Rev. B* **2023**, *108*, 045416.
- (47) Bao, T.; Yu, X.; Wang, X.; Zhao, J.; Su, Y. Photoinduced Carrier Transfer Dynamics in MoSSe/WSSe Vertical and Lateral Heterostructures. *J. Phys. Chem. C* **2023**, *127*, 2078–2087.
- (48) Zheng, Y.; Zhao, H.; Li, W.; Chen, Z.; Zhu, W.; Liu, X.; Tang, Q.; Wang, H.; Wang, C.; Li, Z. Enhanced electron–phonon coupling by delocalizing phonon states for desirable interlayer transfer of excited charges in MoSSe/WS₂ heterobilayer. *Appl. Phys. Lett.* **2023**, *123*.
- (49) Cui, Z.; Yang, K.; Shen, Y.; Yuan, Z.; Dong, Y.; Yuan, P.; Li, E. WS₂ and WSSe bilayer with excellent carrier mobility and power conversion efficiency. *Mat. Sci. Semicon. Proc.* **2023**, *167*, 107820.
- (50) Cen, K.; Yan, S.; Yang, N.; Dong, X.; Xie, L.; Long, M.; Chen, T. The adjustable electronic and photoelectric properties of the WS₂/WSe₂ and WSe₂/WTe₂ van der Waals heterostructures. *Vacuum* **2023**, *212*, 112020.
- (51) Nguyen, C. Q.; Ang, Y. S.; Nguyen, S.-T.; Hoang, N. V.; Hung, N. M.; Nguyen, C. V. Tunable type-II band alignment and electronic structure of C₃N₄/MoSi₂N₄ heterostructure: Interlayer coupling and electric field. *Phys. Rev. B* **2022**, *105*, 045303.

- (52) Ahmad, R.; Ahmad, Z.; Khan, A. U.; Mastoi, N. R.; Aslam, M.; Kim, J. Photocatalytic systems as an advanced environmental remediation: Recent developments, limitations and new avenues for applications. *J. Environ. Chem. Eng.* **2016**, *4*, 4143–4164.
- (53) Janani, G.; Choi, H.; Surendran, S.; Sim, U. Recent advances in rational design of efficient electrocatalyst for full water splitting across all pH conditions. *MRS Bull.* **2020**, *45*, 539–547.
- (54) Fu, C.-F.; Sun, J.; Luo, Q.; Li, X.; Hu, W.; Yang, J. Intrinsic electric fields in two-dimensional materials boost the solar-to-hydrogen efficiency for photocatalytic water splitting. *Nano Lett.* **2018**, *18*, 6312–6317.
- (55) Yuan, Y.-X.; Pan, L.; Wang, Z.-Q.; Zeng, Z.-Y.; Geng, H.-Y.; Chen, X.-R. Two-dimensional Janus pentagonal MSeTe (M= Ni, Pd, Pt): promising water-splitting photocatalysts and optoelectronic materials. *Phys. Chem. Chem. Phys.* **2023**, *25*, 26152–26163.
- (56) Gao, Z.; He, Y.; Xiong, K. Two-dimensional Janus monolayers SPtAZ₂ (A= Si and Ge; Z= N, P, and As): insight into their photocatalytic properties via first-principles calculations. *Phys. Chem. Chem. Phys.* **2024**, *26*, 21173–21185.
- (57) Lv, X.; Wei, W.; Sun, Q.; Li, F.; Huang, B.; Dai, Y. Two-dimensional germanium monochalcogenides for photocatalytic water splitting with high carrier mobility. *Appl. Catal., B* **2017**, *217*, 275–284.
- (58) Liu, H.-Y.; Yang, C.-L.; Wang, M.-S.; Ma, X.-G. Two-dimensional hexaphosphate BiMP₆ (M= Al, Ga, In) with desirable band gaps and ultrahigh carrier mobility for photocatalytic hydrogen evolution. *Appl. Surf. Sci.* **2020**, *517*, 146166.
- (59) Qiao, M.; Chen, Y.; Wang, Y.; Li, Y. The germanium telluride monolayer: a two dimensional semiconductor with high carrier mobility for photocatalytic water splitting. *J. Mater. Chem.A* **2018**, *6*, 4119–4125.

- (60) Ma, Y.; Bao, A.; Guo, X.; Wang, J. Carrier mobility and optical properties of a type-II GaSe/ZnS heterostructure as a photocatalyst: a first-principles study. *Phys. Chem. Chem. Phys.* **2024**, *26*, 14980–14990.
- (61) Alvarez, S. A cartography of the van der Waals territories. *Dalton T.* **2013**, *42*, 8617–8636.
- (62) Guo, G.; Tan, S.; Guo, G.; Xie, Z. Strain-enhanced properties of Janus Si₂PAs monolayer as a promising photocatalyst for the splitting of water: Insights from first-principles calculations. *Colloids Surf. A* **2023**, *659*, 130782.
- (63) Ju, L.; Shang, J.; Tang, X.; Kou, L. Tunable photocatalytic water splitting by the ferroelectric switch in a 2D AgBiP₂Se₆ monolayer. *JACS* **2019**, *142*, 1492–1500.
- (64) Xiao, C.; Sa, R.; Ma, Z.; Cui, Z.; Du, W.; Sun, X.; Li, Q.; Deng, H. High-throughput screening of transition metal single-atom catalyst anchored on Janus MoSSe basal plane for hydrogen evolution reaction. *Int. J. Hydrogen Energ.* **2021**, *46*, 10337–10345.
- (65) Tang, Q.; Jiang, D.-e. Mechanism of hydrogen evolution reaction on 1T-MoS₂ from first principles. *ACS Catal.* **2016**, *6*, 4953–4961.
- (66) Tsai, C.; Chan, K.; Abild-Pedersen, F.; Nørskov, J. K. Active edge sites in MoSe₂ and WSe₂ catalysts for the hydrogen evolution reaction: a density functional study. *Phys. Chem. Chem. Phys.* **2014**, *16*, 13156–13164.